First search for invisible decays of orthopositronium confined in a vacuum cavity

C. Vigo,[1] L. Gerchow,[1] L. Liszkay,[2] A. Rubbia,[1] and P. Crivelli[1,*]

[1]*Institute for Particle Physics and Astrophysics, ETH Zurich, 8093 Zurich, Switzerland*
[2]*IRFU, CEA, University Paris-Saclay F-91191 Gif-sur-Yvette Cedex, France*

(Received 19 March 2018; published 30 May 2018; corrected 25 March 2019)

The experimental setup and results of the first search for invisible decays of orthopositronium (o-Ps) confined in a vacuum cavity are reported. No evidence of invisible decays at a level $\mathrm{Br}(\text{o-Ps} \to \text{invisible}) < 5.9 \times 10^{-4}$ (90% C.L.) was found. This decay channel is predicted in hidden sector models such as the mirror matter (MM), which could be a candidate for dark matter. Analyzed within the MM context, this result provides an upper limit on the kinetic mixing strength between ordinary and mirror photons of $\varepsilon < 3.1 \times 10^{-7}$ (90% C.L.). This limit was obtained for the first time in vacuum free of systematic effects due to collisions with matter.

DOI: 10.1103/PhysRevD.97.092008

I. INTRODUCTION

The origin of dark matter is a question of great importance for both cosmology and particle physics. The existence of dark matter has very strong evidence from cosmological observations [1] at many different scales, e.g. rotational curves of galaxies [2], gravitational lensing [3] and the cosmic microwave background CMB spectrum. The latest Planck mission results [4] provide an accurate estimate of the abundance of baryons $\Omega_b = 0.048$ and cold matter $\Omega_c = 0.258$, leading to an abundance of cold matter ~5 times larger than ordinary matter. The explanation of such observations is one of the strongest hints of the existence of new physics.

Many dark matter (DM) candidates have been hypothesized so far, the most relevant being sterile neutrinos, axions and supersymmetric particles (see Ref. [5] for a detailed, recent review). Supersymmetry is theoretically very attractive since in addition to providing a good candidate for DM (the lightest supersymmetric particle, LSP), it could potentially solve the hierarchy problem [6] and grant unification of gauge couplings at high energies [7], necessary for grand unified theories (GUT). However, all experimental searches have failed to provide any evidence of supersymmetry so far [5,8,9].

Another interesting approach is the concept of a hidden sector (HS) consisting of a $\mathrm{SU}(3)_C \otimes \mathrm{SU}(2)_L \otimes \mathrm{U}(1)_Y$ singlet field [10]. These models extend the SM by introducing a sector which transforms under the new gauge group. Among the many HS scenarios, the mirror sector is a particularly interesting one, featuring a natural dark matter candidate (actually a whole set of candidates) and testable experimental signatures via oscillations of ordinary matter into the HS, as well as a possible explanation of the anomaly reported by the DAMA Collaboration [11].

A. Mirror matter

Mirror matter was originally discussed by Lee and Yang [12] in 1956 as an attempt to preserve parity as an unbroken symmetry of nature after their discovery of parity violation in the weak interaction. They suggested that the transformation in the particle space corresponding to the space inversion $\mathbf{x} \to -\mathbf{x}$ was not the usual transformation P but PR, where R corresponds to the transformation of a particle into a reflected state in the mirror particle space.

The idea was further developed by A. Salam [13] and was clearly formulated in 1966 as a concept of the mirror universe by Kobzarev *et al.* [14]. They proposed a model in which mirror and ordinary matter communicate predominantly through gravity. This concept evolved further into two versions, the symmetric (developed by Foot *et al.* [15]), and the asymmetric (proposed by Berezhiani and Mohapatra [16]). For further historical details, see the review by Okun [17].

The symmetric model provides a viable experimental signature through positronium (Ps). The main idea is that each ordinary particle (i.e. photon or electron) has a mirror particle with the same properties (e.g. mass and charge) but opposite chirality. These mirror particles would be singlets under the standard $\mathrm{G} \equiv \mathrm{SU}(3)_C \otimes \mathrm{SU}(2)_L \otimes \mathrm{U}(1)_Y$ gauge

*paolo.crivelli@cern.ch

interactions [15]. Interactions within mirror particles are identical to their mirror partners: mirror electron and mirror photon will interact with each other in the same way ordinary electron and ordinary photon do. Having opposite chirality, parity conservation is restored at a global level.

Being massive and stable, mirror particles are a very good candidate for dark matter, because they interact with ordinary matter primarily through gravitation [18–22]. However, the model allows other interactions, limited by charge conservation in each sector. Neutral particles and composites can in principle mix with their respective mirror partner, e.g. neutrinos [23], photons [24], the neutral Higgs boson [25,26], neutrons [27–30] or muonium [31]. The photon - mirror photon (γ-γ') mixing mechanism would then induce the Ps-Ps$'$ oscillation through the one-photon virtual annihilation channel of orthopositronium.

Mirror matter can also provide a natural explanation for the similarity between dark matter and ordinary baryonic fractions, $\Omega_{\rm DM} \simeq 5\Omega_{\rm b}$. Although it is true that ordinary and mirror matter would have the same microphysics, that does not necessarily imply they should follow identical cosmological realizations. As pointed out by Berezhiani *et al.* [20], one can assume that the inflationary reheating temperature of the mirror sector T' was lower than the ordinary one T. With this premise, and since the two sectors can only interact very weakly, they would not reach thermal equilibrium with each other in early stages of the Universe and hence would evolve independently during the Universe expansion. Moreover, since baryonic asymmetry (BA) depends on the departure from thermal equilibrium, it is possible that the BA is larger in the mirror sector than in the ordinary one. A temperature ratio $T'/T < 0.2$ could lead to mirror baryonic densities $1 \leq \Omega_{\rm DM}/\Omega_{\rm b} \leq 5$ compatible with the latest Planck mission results [4].

Finally, mirror matter is also an excellent candidate to explain the annual modulation reported by the DAMA Collaboration over 14 annual cycles with the former DAMA/NaI experiment and with the second generation DAMA/LIBRA phase 1 (see [11] and references therein for latest reviews). The observed modulation has a period $T = 0.998(2)$ years and a phase $t_0 = 144(7)$ days, in good agreement with expectations for a dark matter annual modulation signal. These results give model-independent evidence for the presence of dark matter particles in the galactic halo, at a 9.3σ C.L.

Cerulli *et al.* [32] recently showed how the mirror sector can successfully describe such modulation, providing detailed characterizations of several chemical compositions of the mirror sector compatible with cosmological bounds. In particular, for a reference DM density of $\rho_{\rm DM} = 0.3\ {\rm GeV\,cm^{-3}}$ and many different halo temperatures and compositions, they calculate coupling constants in the region $\varepsilon \sim 10^{-9}$, which has not been ruled out by any cosmological limits or direct experimental measurements. For comparison, the upper limit deduced by the successful prediction of the primordial He^4 abundance by the SM is [33],

$$\varepsilon \leq 3 \times 10^{-8}. \tag{1}$$

B. Positronium as a portal into the mirror world

Mirror and ordinary particles interact with each other predominantly by gravity. However, in 1986 Holdom [10] pointed out that any new particle gauged by a new U(1) would couple with a certain constant ε, thus effectively providing fractional charge to the new particles.

Glashow [34] realized that this coupling would lead to a kinetic mixing of photons and mirror photons, described by the interaction Lagrangian density,

$$L = \varepsilon F^{\mu\nu} F'_{\mu\nu}, \tag{2}$$

where $F^{\mu\nu}$ and $F'_{\mu\nu}$ are the field strength tensors for electromagnetism and mirror electromagnetism respectively.

Due to its one-photon virtual annihilation channel, orthopositronium and mirror orthopositronium are connected and the degeneracy between the mass eigenstates is broken [34]. The vacuum eigenstates

$$\frac{\text{o-Ps} + \text{o-Ps}'}{\sqrt{2}} \frac{\text{o-Ps} - \text{o-Ps}'}{\sqrt{2}}$$

are therefore split in energy by $\Delta E = 2h\varepsilon f$, where $f = 8.7 \times 10^4$ MHz is the contribution to the ortho-para splitting from the one-photon virtual annihilation diagram. This splitting leads to Rabi oscillations in which a state that is initially ordinary orthopositronium will oscillate into its mirror partner with a probability

$$\mathcal{P}(\text{o-Ps} \to \text{o-Ps}') = \sin^2 \Omega t, \tag{3}$$

where $\Omega = 2\pi f \varepsilon$ is the oscillation frequency. Note that the Rabi oscillation phenomena does not account for incoherent processes, e.g. collision of o-Ps with matter, which suppress the oscillation probability as discussed in Ref. [35].

Mirror matter having the same microphysics as ordinary matter, o-Ps$'$ will decay into mirror photons, which are very weakly coupled to ordinary matter and thus not detected. Such oscillations will therefore result in an apparent o-Ps $\to$ invisible process with a branching ratio

$$\text{Br}(\text{o-Ps} \to \text{invisible}) = \frac{2\Omega^2}{\Gamma_{\rm SM}^2 + 4\Omega^2}, \tag{4}$$

where $\Gamma_{\rm SM}$ is the Standard Model decay rate of o-Ps [36,37]. Assuming $\varepsilon = 4 \times 10^{-9}$, the oscillation probability is

$$\text{Br}(\text{o-Ps} \to \text{invisible}) = 2 \times 10^{-7}. \tag{5}$$

Note that, within the SM, photonless (and thus invisible) decays of both o-Ps and p-Ps into neutrinos are mediated by

the weak interaction and are heavily suppressed with a branching ratio below 10^{-17} due to the small mass of the positronium atom [38,39].

The above calculations do not consider incoherent processes (e.g. collisions with matter) and the effect of energy shifts induced by electromagnetic fields. Using the density matrix approach, the effect of electromagnetic fields on the branching ratio is shown to be negligible within the region of interest for this experimental search ($E \sim 10$ kV cm^{-1} and $B \sim 80$ G) [35]. On the other hand, collisions of o-Ps with matter play a major role and can be source of large systematic effects and uncertainties [40].

In general, the number of collisions per lifetime will not be a well-defined value but rather a discrete distribution, i.e. a certain fraction of the total o-Ps population f_n will undergo n collisions per lifetime with the corresponding branching ratio Br_n. One can thus calculate the total branching ratio as the weighted average

$$\mathrm{Br} = \sum_{n=0}^{\infty} f_n \cdot \mathrm{Br}_n. \tag{6}$$

C. Current experimental limit on Br(o-Ps → invisible)

Orthopositronium is a sensitive probe to test mirror matter models with two possible experimental signatures, namely the missing energy of the expected SM 1.022 MeV decay or an apparent excess in the o-Ps decay rate compared to QED predictions [41].

Previous measurements of missing energy in o-Ps decays were performed in the presence of matter [42–44], where very high collision rates ($N \sim 10^5$) are expected, resulting in large uncertainties and strong suppression of the oscillation probability. Regarding discrepancies between QED predictions and experimental measurements of the decay rate, the most accurate measurements are still very far from QED precision [36,37]. Although these experiments are performed in a vacuum cavity with low collision rates, the lifetime calculation requires extrapolations to account precisely for the *disappearance* of o-Ps into regions of lower gamma detection efficiency. It is therefore possible that any contribution $\Gamma^{\mathrm{inv}}_{\mathrm{o\text{-}Ps}}$ could be artificially corrected by this extrapolation.

Both signatures have provided so far limits for ε in the range 10^{-6} to 10^{-7} but suffer from large uncertainties. It is thus evident that an experiment with low collision rates (hence in vacuum) but without the need of any extrapolation (hence the missing energy technique) is necessary to confront mirror matter as a candidate to explain the DAMA/LIBRA anomaly.

II. EXPERIMENTAL SETUP

The working principle of our experiment is a vacuum cavity where orthopositronium is confined, surrounded by a hermetic calorimeter to detect the photons expected for a SM decay. The resulting energy spectrum is centered at 1.022 MeV, with a tail due to energy losses and inefficiencies extending down to low energies.

In the case of a o-Ps → o-Ps′ oscillation, the experimental signature would be the absence of this energy deposition in the calorimeter. From simulation, it is possible to estimate the experimental background as the probability to misidentify an actual o-Ps decay (or in general a positron annihilation) as a zero-energy event. Therefore, if oscillations o-Ps → o-Ps′ occur, an excess over the simulation prediction of such zero-energy events would be detected.

Note that o-Ps confined in a vacuum cavity will undergo collisions with the walls, whose rate can be modulated by tuning the o-Ps kinetic energy. A larger collision rate will suppress the o-Ps → o-Ps′ oscillation probability while keeping the background constant. A possible signal observation can thus be cross-checked with controlled collision rate modulation [35].

A. The slow positron beam

The slow positron beam at ETHZ is based on a 120 MBq ^{22}Na radioactive source coupled to a tungsten mesh acting as a moderator providing a flux of $\Phi^{\mathrm{slow}}_{e^+} \sim 15000 e^+ s^{-1}$. Slow (< 3 eV) positrons are electrostatically accelerated to 200 eV and magnetically guided with a set of Helmholtz coils which creates a radially confining field. A high-efficiency tagging system is used to detect the arrival of a positron to the cavity where the positronium converter is placed. The beam is equipped with a velocity selector and a bunching system based on drift tubes and grids where time-dependant potentials are applied [45].

1. The positron tagging system

The tagging of positrons is a crucial feature of the experimental setup. It is used to define the arrival of a positron to the target and therefore serves as the *START* signal for the DAQ. The tagging system is based on a microchannel plate (MCP) which detects secondary electrons (SE) released by a positron hitting the target (Fig. 1).

The positron beam, transversally confined by the magnetic field, is slightly deflected off axis by deflection plates (red), which effectively work as an $E \times B$ filter. Positrons can thus bypass the MCP and are deflected back on axis by an opposite pair of deflection plates (green) and continue their way downstream to the target. They are then accelerated by the target potential U_{T}, where they are implanted and release SE. These electrons are accelerated backwards by the same U_{T} and guided by the same magnetic field. However, when reaching the deflection plates, the electrons are deflected towards the MCP, where they are detected.

This tagging systems presents two important limitations, namely dark counts and detection of other charged particles. Even though the MCP was specifically selected for

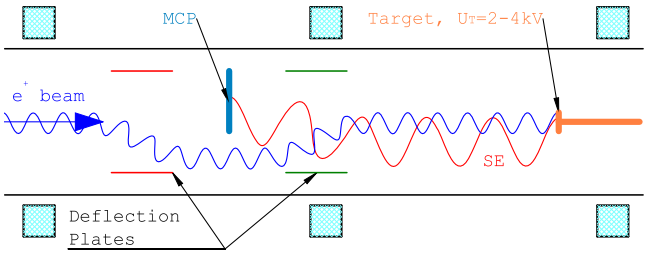

FIG. 1. Positron tagging scheme with a microchannel plate. The positron beam (blue helix, coming from the left) is deflected off axis by the deflection plates (red and green) to bypass the microchannel plate (MCP). Secondary electrons (SE, red helix) are released when the positron impinges the target and guided back and detected by the MCP. Note that the positron and electron trajectories are only sketches, the actual deflection is perpendicular to the drawing plane.

its low dark counts rate (Hamamatsu F4655-12), it is still at the level of 1 Hz. These accidentals are uniformly distributed in time and uncorrelated with the arrival of a positron into the target, and are therefore a source of background. Regarding the detection of other charged particles, it was found that some positrons may annihilate close to or even against the MCP due to transportation inefficiencies. These positrons, or the SE following them, may be detected by the MCP, leading to a trigger accidental correlated with the positron flux, but not with the presence of a positron inside the calorimeter.

2. The chopper

The chopper is a grid placed in front of the tungsten moderator and set above the moderator potential $U_M = 200$ V to constantly block the low energy positrons. Driven by a global clock, the chopper is pulsed down below U_M, thus letting through the positrons during a time window $t_W = 300$ ns, at a frequency $f = 333$ kHz ($T = 3$ μs). The chopping system suppresses positron pileup, i.e. the presence of more than one positron in the cavity within the same event, which introduces a signal inefficiency. The total signal efficiency can be measured using a trigger uncorrelated with the positron beam and was found to be $\eta_S = 92.1\%$.

3. The buncher

The 300 ns positron pulse is compressed into a few ns by means of a double-gap buncher [45] sketched in Fig. 2 to increase the signal-to-noise ratio and reduce triggering-related background, e.g. MCP noise. A positron arriving at gap 1 is accelerated by the time-dependent potential difference so that late positrons will acquire a larger velocity. If the potential in the buncher is set properly, a linear velocity distribution can be achieved, producing an ideal compression into a shorter positron bunch. The same

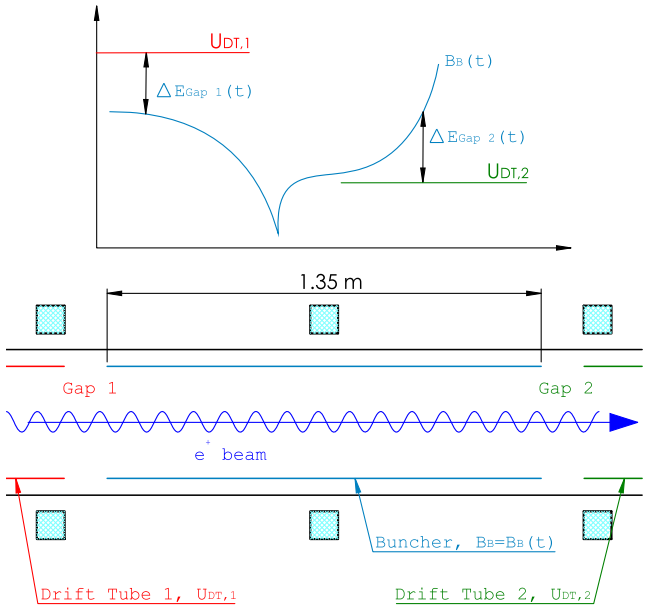

FIG. 2. Positron bunching scheme.

process is repeated at gap 2, the goal being to compress the bunch as much as possible when it reaches the target.

The initial 300 ns bunches are compressed to 14 ns FWHM pulses (Fig. 3). The energy range of the positrons is given by

$$U_M - U_B < E_{e^+} < U_M + U_B, \tag{7}$$

where $U_B = 60$ V and $U_M = 200$ V are the buncher amplitude and the moderator potential.

4. The reimplantation electrode

When positrons reach the positronium cavity, they are accelerated to a few keV and impinge on the target. They quickly slow down and diffuse in the bulk, where they will generally pick up an electron. However, a positron can also reach the surface again before losing all its kinetic energy

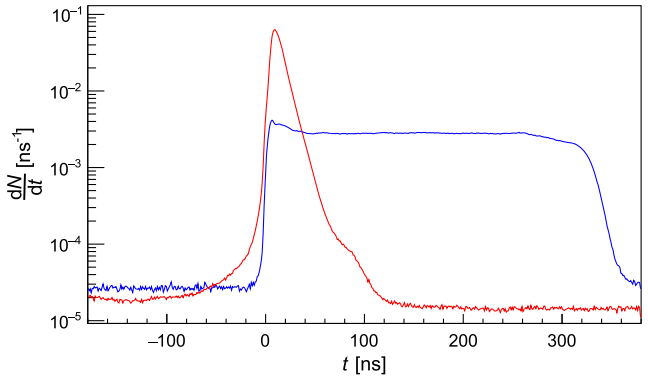

FIG. 3. Time distribution of unbunched (blue) and bunched (red) positrons on the target.

and escape into vacuum, i.e. it can be backscattered [35]. The energy range of these positrons is

$$E_{e^+}^{back} \in [0, U_T + U_M + U_B], \quad (8)$$

where U_T is the target potential and $U_M + U_B$ is the maximum initial energy from Eq. (7). Backscattered positrons with enough energy to escape the cavity ($E_{e^+}^{back} > U_T$) are expected at a level 10^{-4} (see Sec. II D 3), becoming a source of background.

A reimplantation electrode is placed at the end of the beam line, before the cavity, to ensure no backscattered positron escapes the cavity. The electrode is set to a low potential, below the minimum positron energy $U_M - U_B$. After the compressed bunch of positrons has passed through, the electrode potential is raised above the maximum positron energy, $U_M + U_B$, blocking all backscattered positrons and reducing the background below 10^{-6} (see Sec. II D 3).

B. The orthopositronium cavity

1. Orthopositronium production in vacuum

Positronium production in vacuum is achieved with a porous film where a positron impinges and captures an electron from the bulk to form o-Ps, which diffuses through the porous structure back into vacuum. Different samples that can be used to produce positronium were studied and characterized [46–49], the most promising positronium converters for this experiment being thin silica films prepared on a rigid substrate with a nonionic surfactant, which is later removed by heating at 450 °C to obtain the porous structure.

The samples were prepared on a 110 μm thick, 15 mm diameter borosilicate disc with a 10 nm layer of gold deposited in the opposite face of the disc to improve conductivity. This thin substrate reduces photon energy losses which could lead to background. The main features of these films (see Table I) are a high and constant yield of o-Ps in vacuum ($y_{o\text{-}Ps} \sim 30\%$) for the implantation energy interval 2 to 4 keV and an o-Ps re-emission energy dependent on positron implantation energy [49].

The positronium cavity consists of a 0.7 mm thick, 17 mm diameter aluminum pipe where the positronium converter is attached and set to a potential U_T to accelerate incoming positrons. A thin aluminum wire (core diameter of 200 μm) was coiled around the cavity to create a homogeneous magnetic field to guide positrons into the cavity and extract secondary electrons.

TABLE I. Orthopositronium yield $y_{o\text{-}Ps}$ and mean kinetic energy $E_{o\text{-}Ps}$ from Ref. [49] and estimated average number of collisions per lifetime N_{coll} from simulation, for different positron implantation energies E_{e^+}. The expected branching ratio Br(o-Ps → o-Ps′) is calculated according to Eq. (6), assuming $\varepsilon = 4 \times 10^{-9}$.

E_{e^+} [keV]	$y_{o\text{-}Ps}$	$E_{o\text{-}Ps}$ [meV]	N_{coll}	Br(o-Ps → o-Ps′)
2	30%	440	3.37	1.1×10^{-7}
3	30%	220	2.42	9.8×10^{-8}
4	29%	130	1.87	8.3×10^{-8}

2. Signal modulation

In case of signal observation, a key feature of the experiment is the possibility to check that the origin of the signal is due to new physics rather than an underestimation of the background. Due to the signal suppression induced by collisions of o-Ps with matter, one can modulate the signal by tuning the velocity of o-Ps and thus the rate of collisions [35]. Figure 4 shows the distribution of events with different number of total collisions per lifetime at different positronium kinetic energies, corresponding to the implantation energies 4 keV, 3 keV and 2 keV from Table I. As expected, more energetic positronium (from a shallower implanted positron) shows a larger frequency of many-collisions events. As a guide for the eye, the branching ratio for the different collision rates is also plotted, assuming $\varepsilon = 4 \times 10^{-9}$. Note that events with many collisions with the cavity have a much lower probability to oscillate into o-Ps′.

For each o-Ps kinetic energy, one can then calculate the average branching ratio with Eq. (6). The difference between such branching ratios for two given o-Ps energies provides the modulation of the oscillation signal.

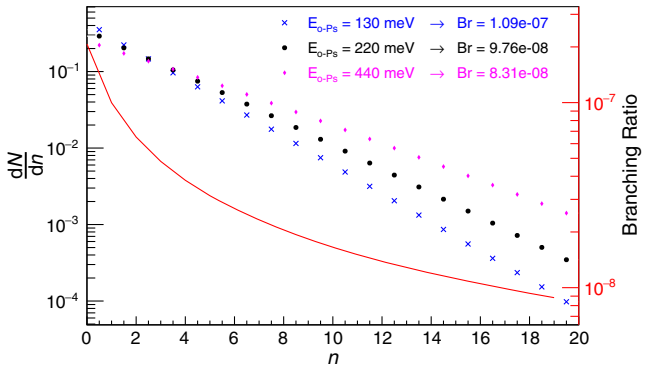

FIG. 4. Distribution of events with total number of o-Ps collisions per lifetime n for different o-Ps emission energies, from GEANT4 simulation. Red solid line shows the branching ratio for the process o-Ps → o-Ps′ for a coupling constant $\varepsilon = 4 \times 10^{-9}$, electric field $E = 10$ V cm^{-1} and magnetic field $B = 70$ G. Dotted points are frequencies of events with n collisions from simulations with different o-Ps emission energies. The averaged branching ratios are calculated according to Eq. (6) for each monoenergetic case.

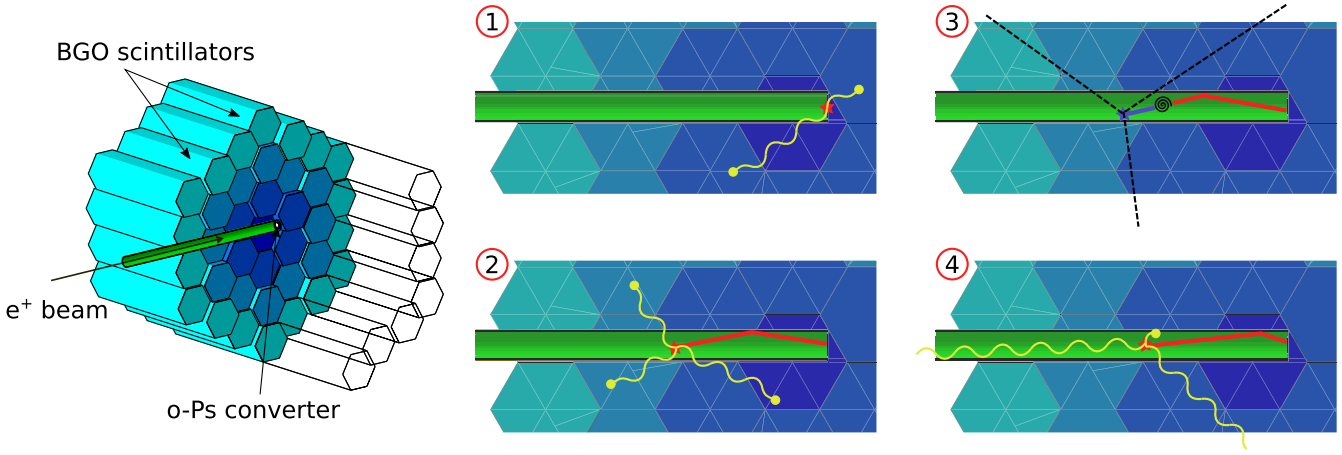

FIG. 5. *Left*: sectional view of the calorimeter with the vacuum cavity and the positronium converter. Some scintillators from the cut side are shown as wire-frames for reference. *Right*: sketches of possible events 1) prompt annihilation and p-Ps decay into two back-to-back 511 keV photons. 2) o-Ps decay into three photons. 3) o-Ps → o-Ps′ oscillation, o-Ps′ then decays into three γ' which are not detected in the ECAL. 4) background event where a photon is absorbed in the cavity and two photons escape the ECAL.

C. The calorimeter

The experimental signature of o-Ps → o-Ps′ is the absence of energy deposition in a hermetic calorimeter (ECAL) surrounding the o-Ps cavity. The calorimeter consists of 92 BGO ($Bi_{12}GeO_{20}$) scintillators placed in a two-halves honeycomb structure with an aperture to accommodate the positronium cavity (Fig. 5). Each individual detector is a scintillating crystal (a 200 mm long and 55 mm wide hexagonal prism) and a thin wrapping around the crystal to increase light collection, improve energy resolution and reduce cross talk between neighboring detectors. Each detector is coupled to a photomultiplier tube (PMT) which collects the scintillating light, producing an amplified electrical signal proportional to the original photon energy.

The detector is mounted inside a light-tight PVC black box to avoid the PMTs detecting natural light as a signal. Since the gains of both BGO scintillators and PMTs are very sensitive to temperature (effective temperature coefficient estimated to be $-1.38\%\,°\,C^{-1}$ [50]), the PVC box is equipped with two copper plates coupled to a temperature controlled water circuit, resulting in the long-term stability necessary for the data taking. To improve heat extraction from the cavity solenoid, precooled pressurized air is fed into the ECAL, greatly increasing convection efficiency.

Each PMT signal is read out individually via a set of CAEN V792 QDC modules, which integrate the current over a time $t_G = 3\ \mu s$ after the t_{START} signal from the MCP. The probability of o-Ps decaying after t_G is

$$S = \int_{t_G}^{\infty} \frac{1}{\tau_{\text{o-Ps}}} \exp\left(-\frac{t}{\tau_{\text{o-Ps}}}\right) dt = \exp\left(-\frac{t_G}{\tau_{\text{o-Ps}}}\right) = 6.7 \times 10^{-10} \tag{9}$$

well below the expected sensitivity.

The o-Ps → o-Ps′ signal is defined as the absence of energy deposition in any crystal. Due to finite energy resolution and contribution of electronics and PMT noise, one must set for each BGO i a certain threshold $E_{T,i}$ below which the energy deposition is considered to be zero. These thresholds were individually picked to minimize both signal inefficiency (i.e. the probability to misidentify a zero-energy event as a SM decay) and energy losses (energy depositions in a single BGO below $E_{T,i}$ will not be accounted for, leading to possible background).

The individual energy depositions are thus summed up to obtain the total energy E_{ECAL}

$$E_{\text{ECAL}} = \sum_{i}^{92} \begin{cases} 0 & \text{if } E_i < E_{T,i} \\ E_i & \text{if } E_i \geq E_{T,i} \end{cases}. \tag{10}$$

Therefore the signal (zero-energy compatible events) is defined as those events with $E_{ECAL} = 0$.

D. Background sources

The four following sources of background have been identified:

1. Trigger accidentals

Trigger accidentals happen when an MCP signal is detected without the presence of a positron in the cavity, and they represent the largest background contribution. Three different types were found

(i) MCP dark counts (<1 Hz), which are uniformly distributed in time and unrelated to neither the positron beam nor the implantation energy.
(ii) Positron-related triggers. Due to beam transportation inefficiencies, some positrons may annihilate close to the MCP or even against it. The corresponding

secondary electrons or even the annihilation photons can be detected by the MCP, leading to a time- and beam-dependent background.

(iii) Electrons released from the positronium converter due to the strong electric field, which are transported upstream as if they were secondary electrons. This contribution is uniformly distributed in time but depends on the implantation energy.

Trigger accidentals are the dominant background ($>10^{-4}$), but its rate can be experimentally determined, as will be shown later.

2. Calorimeter

The calorimeter was designed to ensure high hermeticity and minimize photon energy losses, verified by a detailed GEANT4 [51] simulation of the complete setup. Energy depositions in dead material, i.e. anything besides the scintillators, increase the probability to misidentify a positron annihilation as a zero-energy compatible event, especially when detector efficiency and energy resolution are taken into account. The simulation considers the contribution from all structural elements of the cavity (e.g. the pipe, the solenoid or the o-Ps converter) as well as the scintillator wrappings. The kinetic energy of o-Ps is another key parameter: faster o-Ps is more likely to decay further upstream, where hermeticity decreases (see Fig. 5). With a kinetic energy $E_{\text{o-Ps}} = 440$ meV, corresponding to the shallowest implantation energy $E_{e^+} = 2$ keV, the total background due to energy losses and hermeticity is at a level of 10^{-7}, below the experimental sensitivity.

3. Backscattered positrons

As explained in Sec. II A 4, positron backscattering is a very well-known process which may lead to a tagged positron escaping the confinement cavity. A GEANT4 simulation was used to obtain the positron backscattering fraction, as well as its energy and angular distribution, based on Ref. [52]. The trajectory of a backscattered positron inside the vacuum pipe was then simulated with the beam optics package SIMION [53], reproducing the electric and magnetic fields in the vacuum cavity. Table II shows the simulated backscattering and escape probabilities at different implantation energies, which were at a level of 10^{-7} in very good agreement with measurements performed without the reimplantation electrode. This background can be suppressed below the experimental sensitivity with the use of the abovementioned reimplantation electrode.

4. Fast backscattered o-Ps

Orthopositronium can be emitted from the converter with large kinetic energy (peaking around 15 eV) due to backscattered positrons which capture an electron before exiting the surface [35]. A very energetic o-Ps is more likely to escape the high-efficiency detection volume. This possibility has been studied using a GEANT4 simulation and similar assumptions from Ref. [35]: for o-Ps with kinetic energy below its binding energy (6.8 eV), the annihilation probability via pickoff when it collides with the pipe is very conservatively assumed to be zero, and 100% otherwise above the dissociation threshold [54].

TABLE II. Simulated positron backscattering fraction and escape probabilities, with and without the reimplantation electrode, at different positron implantation energies E_{e^+}.

E_{e^+} [keV]	Backscattered fraction [%]	Background	
		Without electrode	With electrode
2	5.861(7)	$1.79(4) \times 10^{-4}$	$< 4.5 \times 10^{-6}$
3	6.882(8)	$1.28(4) \times 10^{-4}$	$< 3.7 \times 10^{-6}$
4	7.484(9)	$1.02(3) \times 10^{-4}$	$< 4.1 \times 10^{-6}$

TABLE III. Simulated escape probabilities of fast backscattered o-Ps.

o-Ps energy [eV]	Escape probability ξ
3	$3.392(4) \times 10^{-4}$
6	$1.238(3) \times 10^{-3}$
7	$5.4(1) \times 10^{-5}$
20	$1.17(2) \times 10^{-4}$
100	$2.17(2) \times 10^{-4}$

Table III shows the escape probability ξ for some o-Ps kinetic energy. As expected, larger kinetic energies of o-Ps lead to a higher escape probability. However, note that above $E_{e^+} = 6.8$ eV the pickoff probability function changes from 0% to 100%, and therefore the escaping probability is suppressed.

This background estimation has to be integrated over the whole backscattered o-Ps energy spectrum, which can be assumed to be a Landau distribution peaked at 15 eV, the maximum of the e^- capture cross section [35]. A rough estimation of the total escape probability $\xi_{\text{o-Ps}}$ gives $\xi_{\text{o-Ps}} < 10^{-4}$. The resulting background is then calculated as

$$B_{\text{o-Ps}} = f_{\text{back. o-Ps}} \cdot \xi_{\text{o-Ps}}, \tag{11}$$

where $f_{\text{back o-Ps}}$ is the fraction of incident positrons leading to fast backscattered o-Ps. This fraction decreases at larger positron implantation energies and can be estimated to be $f_{\text{back o-Ps}} < 1\%$ already at $E_{e^+} = 2$ keV [54], resulting in a background below 10^{-6}.

III. RESULTS

Data were collected for positron implantation energies 2 to 4 keV for several days (see Table IV). Each data set

TABLE IV. Chronological relation of data sets, with positron implantation energy E_{e^+} and acquisition times t_{acq} (beam on) and t^b_{acq} (beam off).

Run ID	E_{e^+} [keV]	t_{acq} [h]	t^b_{acq} [h]
1	2.0	13.6	7.9
2	3.0	16.7	11.8
3	4.0	18.2	18.7
4	3.5	10.9	26.9
5	3.0	41.9	5.4

consists of a collection of events, for which the event time t (time difference between positron tagging and the chopper pulse measured with a CAEN V1290N Time-to-Digital Converter with 250 ps resolution) and the energy depositions E_i in every scintillator are recorded. The normalized event rate is defined as

$$\hat{\Phi} = \frac{1}{t_{acq}} \frac{dN}{dt}, \tag{12}$$

where t_{acq} is the acquisition time from Table IV. Figure 6 shows the normalized event rate of all events (in blue) when the target is set to 1750 V (top) and when it is grounded (bottom). The red line corresponds to the subset of zero-energy compatible events, i.e. events with no energy deposition in any scintillator, $E_{ECAL} = 0$.

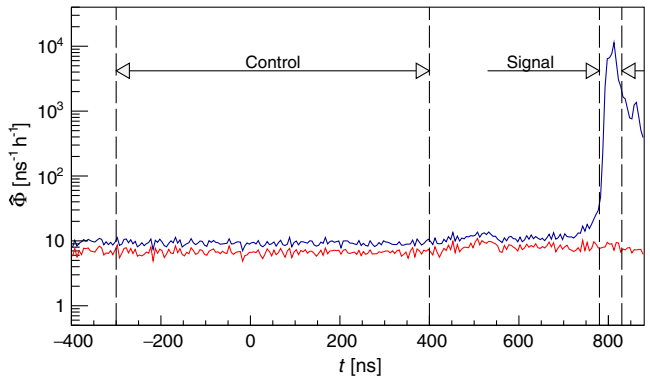

(a) Target at 1750 V.

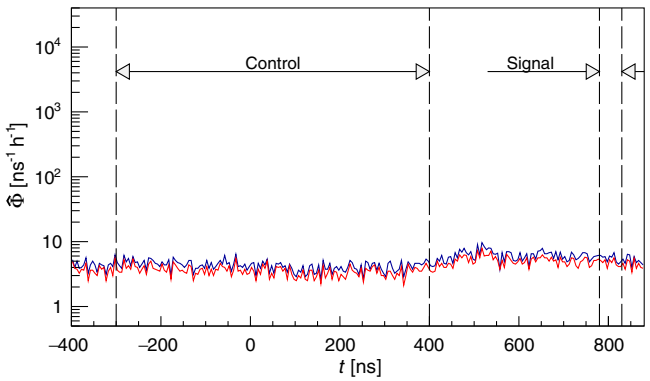

(b) Target grounded.

FIG. 6. Time distribution of all (blue) and zero-energy (red) events is shown when the target is set at $U_T = 1750$ V (top) and when it is grounded (bottom).

The grounded target configuration provides an excellent background estimation, because secondary electrons released by the incoming positrons are not accelerated and therefore do not reach the MCP. The small fraction of events with $E_{ECAL} > 0$ (difference between blue and red lines) is due to inefficiencies in the calorimeter, e.g. cosmic rays and electronics noise, which were measured to be ~10%.

When a negative potential is applied to the target, positrons are tagged and a clear excess of total events is observed around $t = 815$ ns. The positron pulse timing depends on the chopper and bunching configuration (see Sec. II A), as well as the implantation energy, due to secondary electrons reaching faster the MCP at higher target potentials. The width of the signal region is chosen to maximize the sensitivity to ε, optimizing the ratio between total events (blue) and background events (red) in Fig. 6. The signal region is thus defined as the narrow time window where the positron pulse is expected and where an excess of zero-energy compatible events is searched.

A. Background estimation

The background estimation provides the number of zero-energy compatible events N_B to be expected in the signal region for each measurement. The background rate can be calculated as the combination of three normalized rates obtained in the control and signal regions defined in Fig. 6. One can then define, according to Eq. (12), the following mean normalized rates:

(i) Target ON, control region: $\hat{\Phi}_{B,1}$
(ii) Target OFF, control region: $\hat{\Phi}_{B,2}$
(iii) Target OFF, signal region: $\hat{\Phi}_{B,3}$

$\hat{\Phi}_{B,1}$ accounts for all background contributions that are uniformly distributed in time, e.g. MCP dark counts and electrons released due to the applied target potential U_T. When the target is off, the contribution from positrons annihilating at the MCP or its vicinity and being detected is not modified, which can be therefore estimated by the difference $\hat{\Phi}_{B,3} - \hat{\Phi}_{B,2}$. This value was found to depend on the beam configuration used to guide the positrons to the target, which has to be adjusted for each target potential. It was thus necessary to take a background measurement for each implantation energy. The expected background rate at the signal region with target ON is thus,

$$\hat{\Phi}_B = \hat{\Phi}_{B,1} + \hat{\Phi}_{B,3} - \hat{\Phi}_{B,2}. \tag{13}$$

The expected number of background events N_B can then be calculated as

$$N_B = \hat{\Phi}_B \cdot \Delta t_S \cdot t_{acq}, \tag{14}$$

TABLE V. Expected background events N_B, observed events N_O and total events N_{tot} in the signal region for each implantation energy $E_{o\text{-}Ps}$.

$E_{o\text{-}Ps}$ [keV]	N_B	N_O	N_{tot}
2.0	158(36)	151(12)	$2.038(5) \times 10^5$
3.0	357(55)	395(20)	$3.256(6) \times 10^5$
3.0	630(130)	627(25)	$6.900(8) \times 10^5$
3.5	306(32)	316(18)	$1.566(4) \times 10^5$
4.0	1616(81)	1534(39)	$3.777(6) \times 10^5$

where Δt_S is the signal region width from Fig. 6 and t_{acq} is the acquisition time from Table IV. Table V shows the resulting expected number of background events and the observed events for all runs, which were found to be compatible within one standard deviation. It is thus concluded that no excess of zero-energy compatible events was observed at any positron implantation energy.

B. Limits on branching ratios

Since no signal events were observed above the expected background, upper limits on the branching ratio of the processes $e^+ \to$ invisible and o-Ps $\to$ invisible can be set. In the presence of a known background N_B and a certain signal N_S, the number of expected events N_E is

$$N_E = N_S + N_B = N_{tot} \cdot \eta_S \cdot \mathrm{Br} + N_B, \qquad (15)$$

where $\eta_S = 92.1\%$ is the signal detection efficiency, N_{tot} is the total number of events and Br the branching ratio of the process.

The number of observed events N_O can be assumed to follow a Poisson distribution due to the counting nature of the experiment, and all uncertainties are taken to be normally distributed. Using a Bayesian approach with a flat prior distribution, upper limits can be extracted for single and multiple data sets [55,56]. The resulting limits on the branching ratios are shown in Table VI.

TABLE VI. Summary of limits on branching ratios Br($e^+ \to$ inv) and Br(o-Ps $\to$ inv), and resulting limits on the coupling constant ε. All limits are given with 90% C.L.

	Br($e^+ \to$ inv)	Br(o-Ps $\to$ inv)	ε
E_{e^+} [keV]	$[10^{-4}]$	$[10^{-4}]$	$[10^{-7}]$
2.0	3.2	11.2	4.6
3.0	4.2	15.5	5.0
3.0	3.5	12.9	4.6
3.5	4.8	17.8	5.2
4.0	3.2	12.0	4.2
Combined	1.7	5.9	3.1

C. Limit on mixing strength ε

Limits on the coupling constant ε can be extracted from Br(o-Ps $\to$ invisible). For each implantation energy E_{e^+}, one can assume the corresponding o-Ps mean emission energy extracted from the TOF data [49] and obtain the discrete frequency distribution of collision rate from simulation (Fig. 4). Iteratively solving Eq. (6) yields then the upper limits on ε shown in Table VI. The data for the relevant o-Ps energies were summarized in Table I. The uncertainties in the o-Ps yield and energy were taken from Ref. [49] and, from simulations, the resulting uncertainties in ε were found to be below 1% and thus can be neglected.

D. Comparison with Monte Carlo simulations

The expected hermeticity of the ECAL is $\sim 10^{-8}$, well below the experimental background level presented in Table V. In order to assess the simulation prediction, the probability for a single 511 keV photon to escape is a good estimate because the background due to trigger accidentals is greatly suppressed by localizing the 511 KeV energy of a positron annihilation photon in one BGO, the trigger BGO. One can then define the energy deposition E_{ECAL} in the rest of the calorimeter, i.e. E_{ECAL} accounts for energy depositions in all crystals except the trigger BGO. The selection of this trigger BGO also allows to test hermeticity isotropy over the entire ECAL.

Figure 7 shows the energy E_{ECAL} spectrum when a 511 ± 60 keV photon is localized in a BGO of the most inner layer at an implantation energy $E_{e^+} = 4$ keV. The red line is the simulated spectrum, assuming a monoenergetic fraction of orthopositronium $f_{o\text{-}Ps} = 29\%$ with kinetic energy $E_{o\text{-}Ps} = 130$ meV (see Table I). Note the good agreement between data and simulation, especially the width of the 511 keV peak (i.e. the simulation correctly models the detectors response) and the low energy tail,

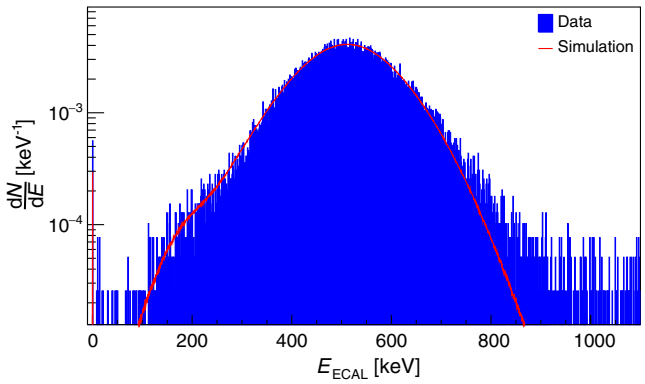

FIG. 7. Energy spectrum (blue) of the ECAL when a 511 ± 60 keV photon is localized in an inner BGO with an implantation energy $E_{e^+} = 4$ keV, and simulation (red line) with a monoenergetic fraction $f_{o\text{-}Ps} = 29\%$ and kinetic energy $E_{o\text{-}Ps} = 130$ meV.

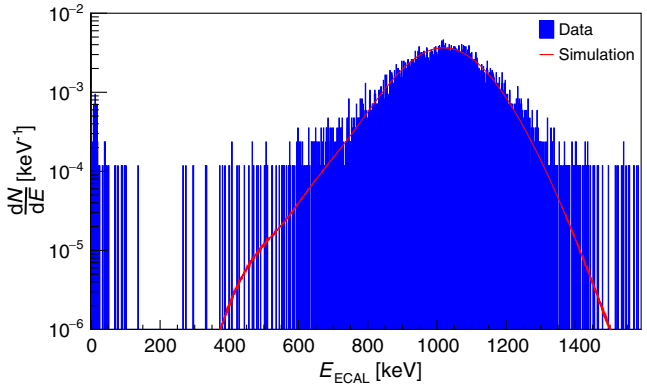

FIG. 8. Total energy spectrum (blue) of the ECAL at an implantation energy $E_{e^+} = 4$ keV, and simulation (red line) with a monoenergetic fraction $f_{o\text{-}Ps} = 29\%$ and kinetic energy $E_{o\text{-}Ps} = 130$ meV.

which is the most interesting when assessing ECAL hermeticity.

On the other hand, the comparison of the total energy E_{ECAL} spectrum shown in Fig. 8 can only be qualitative due to the background from trigger accidentals, i.e. only general agreement of the spectrum shape and low energy tail can be checked. It is worth noting the clear separation between the low energy tail due to ECAL inefficiencies (e.g. energy losses and photon escape) and the tail due to trigger accidental and signal inefficiency (i.e. a trigger accidental with little energy deposition due to PMT noise). The fairly good match between the ECAL inefficiency tail and the simulation increases the confidence in simulation predictions on the ECAL hermeticity.

IV. CONCLUSIONS

In this paper the results of the first search for an invisible decay of o-Ps confined in a vacuum cavity were presented. No event above the expected background was found in the signal region, and thus an upper limit for the branching ratio was obtained,

$$\mathrm{Br}(\text{o-Ps} \to \text{invisible}) < 5.9 \times 10^{-4} \quad (90\%\text{C.L.}).$$

This result, analyzed in the context of the mirror matter model, provides an upper limit on the mirror and ordinary photons kinetic mixing strength

$$\varepsilon < 3.1 \times 10^{-7} \quad (90\%\text{C.L.})$$

obtained for the first time free of systematic effects due to the absence of collisions of o-Ps with matter.

The main limitation of the experimental sensitivity is the background arising from positron tagging accidentals, which could be overcome with e.g. a higher positron flux or an improved confinement cavity and tagging system [35]. Such upgrades would improve the sensitivity to $\varepsilon \sim 10^{-9}$, below the current limit from big bang nucleosynthesis constraints ($\varepsilon \leq 3 \times 10^{-8}$), which would confront directly the interpretation of the DAMA/LIBRA claim of a signal observation in terms of mirror matter.

ACKNOWLEDGMENTS

We wish to thank S. Gninenko and A. Belov for their essential contributions to the first stages of the experiment. We are grateful to A. Battaglioni and H. Yarar for their help in the construction of the experimental setup and in the data taking. We thank R. Vallery and D. Cooke for their valuable discussions and helpful comments. This work was supported by the ETH Zurich Grant No. ETH-35-14-2.

[1] G. Bertone, D. Hooper, and J. Silk, Phys. Rep. **405**, 279 (2005).
[2] K. G. Begeman, A. H. Broeils, and R. H. Sanders, Mon. Not. R. Astron. Soc. **249**, 523 (1991).
[3] R. Massey, T. Kitching, and J. Richard, Rep. Prog. Phys. **73**, 086901 (2010).
[4] P. A. R. Ade *et al.* (Planck Collaboration), Astron. Astrophys. **594**, A13 (2016).
[5] C. Patrignani *et al.* (Particle Data Group), Chin. Phys. C **40**, 100001 (2016).
[6] S. P. Martin, Adv. Ser. Dir. High Energy Phys. **21**, 1 (2010); **18**, 1 (1998).
[7] J. Ellis, S. Kelley, and D. Nanopoulos, Nucl. Phys. **B373**, 55 (1992).
[8] G. Aad *et al.* (ATLAS Collaboration), J. High Energy Phys. 10 (2015) 134.
[9] V. Khachatryan *et al.* (CMS Collaboration), J. High Energy Phys. 05 (2015) 078.
[10] B. Holdom, Phys. Lett. **166B**, 196 (1986).
[11] R. Bernabei *et al.*, Bled Workshops Phys. **17**, 1 (2016); EPJ Web Conf. **136**, 05001 (2017).
[12] T. D. Lee and C. N. Yang, Phys. Rev. **104**, 254 (1956).
[13] A. Salam, Il Nuovo Cimento **5**, 299 (1957).
[14] I. Kobzarev, L. Okun, and I. Pomeranchunk, Yad. Fiz. **3**, 1154 (1966); [Sov. J. Nucl. Phys. **837**, 837 (1966)].
[15] R. Foot, H. Lew, and R. Volkas, Phys. Lett. B **272**, 67 (1991).

[16] Z. G. Berezhiani and R. N. Mohapatra, Phys. Rev. D **52**, 6607 (1995).
[17] L. B. Okun, Phys. Usp. **50**, 380 (2007).
[18] S. I. Blinnikov and M. Y. Khlopov, Yad. Fiz. **36**, 809 (1982); [Sov. J. Nucl. Phys. **36**, 472 (1982)].
[19] S. I. Blinnikov and M. Y. Khlopov, Astron. Zh. **50**, 632 (1983); [Sov. Astron. **27**, 371 (1983)].
[20] Z. Berezhiani, D. Comelli, and F. L. Villante, Phys. Lett. B **503**, 362 (2001).
[21] Z. Berezhiani, P. Ciarcelluti, D. Comelli, and F. L. Villante, Int. J. Mod. Phys. D **14**, 107 (2005).
[22] S. I. Blinnikov, Phys. At. Nucl. **73**, 593 (2010).
[23] R. Foot and R. R. Volkas, Phys. Rev. D **61**, 043507 (2000).
[24] R. Foot, A. Y. Ignatiev, and R. R. Volkas, Phys. Lett. B **503**, 355 (2001).
[25] R. Barbieri, T. Gregoire, and L. J. Hall, arXiv:hep-ph/0509242.
[26] A. Y. Ignatiev and R. R. Volkas, Phys. Lett. B **487**, 294 (2000).
[27] Z. Berezhiani and L. Bento, Phys. Rev. Lett. **96**, 081801 (2006).
[28] G. Ban *et al.*, Phys. Rev. Lett. **99**, 161603 (2007).
[29] A. P. Serebrov *et al.*, Phys. Lett. B **663**, 181 (2008).
[30] Y. N. Pokotilovski, Phys. Lett. B **639**, 214 (2006).
[31] S. N. Gninenko, N. V. Krasnikov, and V. A. Matveev, Phys. Rev. D **87**, 015016 (2013).
[32] R. Cerulli, P. Villar, F. Cappella, R. Bernabei, P. Belli, A. Incicchitti, A. Addazi, and Z. Berezhiani, Eur. Phys. J. C **77**, 83 (2017).
[33] E. D. Carlson and S. L. Glashow, Phys. Lett. B **193**, 168 (1987).
[34] S. Glashow, Phys. Lett. **167B**, 35 (1986).
[35] P. Crivelli, A. Belov, U. Gendotti, S. Gninenko, and A. Rubbia, J. Instrum. **5**, P08001 (2010).
[36] G. S. Adkins, R. N. Fell, and J. Sapirstein, Phys. Rev. Lett. **84**, 5086 (2000).
[37] R. S. Vallery, P. W. Zitzewitz, and D. W. Gidley, Phys. Rev. Lett. **90**, 203402 (2003).
[38] A. Pokraka and A. Czarnecki, Phys. Rev. D **94**, 113012 (2016).
[39] A. Czarnecki and S. G. Karshenboim, in *High energy physics and quantum field theory. Proceedings, 14th International Workshop, QFTHEP'99, Moscow, Russia, May 27-June 2, 1999,* edited by B. B. Levchenko and V. I. Savrin (1999) p. 538, arXiv:hep-ph/9911410 (to be published).
[40] S. V. Demidov, D. S. Gorbunov, and A. A. Tokareva, Phys. Rev. D **85**, 015022 (2012).
[41] S. N. Gninenko, Phys. Lett. B **326**, 317 (1994).
[42] G. S. Atoyan, S. N. Gninenko, V. I. Razin, and Y. V. Ryabov, Phys. Lett. B **220**, 317 (1989).
[43] T. Mitsui, R. Fujimoto, Y. Ishisaki, Y. Ueda, Y. Yamazaki, S. Asai, and S. Orito, Phys. Rev. Lett. **70**, 2265 (1993), see Ref. [41] for a correction to the coupling constant limit due to collisions of o-Ps with matter.
[44] A. Badertscher, P. Crivelli, W. Fetscher, U. Gendotti, S. N. Gninenko, V. Postoev, A. Rubbia, V. Samoylenko, and D. Sillou, Phys. Rev. D **75**, 032004 (2007).
[45] N. Alberola, T. Anthonioz, A. Badertscher, C. Bas, A. Belov, P. Crivelli, S. Gninenko, N. Golubev, M. Kirsanov, A. Rubbia, and D. Sillou, Nucl. Instrum. Methods Phys. Res., Sect. A **560**, 224 (2006).
[46] L. Liszkay, C. Corbel, P. Perez, P. Desgardin, M.-F. Barthe, T. Ohdaira, R. Suzuki, P. Crivelli, U. Gendotti, A. Rubbia, M. Etienne, and A. Walcarius, Appl. Phys. Lett. **92**, 063114 (2008).
[47] L. Liszkay, C. Corbel, P. Perez, P. Desgardin, M. F. Barthe, T. Ohdaira, R. Suzuki, P. Crivelli, U. Gendotti, A. Rubbia, M. Etienne, and A. Walcarius, Mater. Sci. Forum **607**, 30 (2009).
[48] D. B. Cassidy, P. Crivelli, T. H. Hisakado, L. Liszkay, V. E. Meligne, P. Perez, H. W. K. Tom, and A. P. Mills, Phys. Rev. A **81**, 012715 (2010).
[49] P. Crivelli, U. Gendotti, A. Rubbia, L. Liszkay, P. Perez, and C. Corbel, Phys. Rev. A **81**, 052703 (2010).
[50] P. Wang, Y. Zhang, Z. Xu, and X. Wang, Sci. China Phys. Mech. Astron. **57**, 1898 (2014).
[51] S. Agostinelli *et al.* (GEANT4 Collaboration), Nucl. Instrum. Methods Phys. Res., Sect. A **506**, 250 (2003).
[52] H. Shi-Juan, P. Zi-Wen, L. Jian-Dang, H. Rong-Dian, and Y. Bang-Jiao, Chin. Phys. B **24**, 107803 (2015).
[53] D. A. Dahl, Int. J. Mass Spectrom. **200**, 3 (2000).
[54] D. W. Gidley, D. N. McKinsey, and P. W. Zitzewitz, J. Appl. Phys. **78**, 1406 (1995).
[55] T. Hebbeker, Calculating upper limits with Poisson statistics, L3 Note 2633, 2001.
[56] C. Vigo, Search for invisible decay channels of positronium confined in a vacuum cavity, Ph.D. Thesis, ETH Zurich, 2017.

Correction: Conversion errors for the values 5.9×10^{-4} appearing in the abstract and conclusion section and typographical errors have been fixed.